# The big problem of small particles

Alicia Weibel, Renaud Bouchet, Florence Boulc'H, Philippe Knauth

# The Big Problem of Small Particles: A Comparison of Methods for Determination of Particle Size in Nanocrystalline Anatase Powders

**A. Weibel, R. Bouchet, F. Boulc'h, and P. Knauth**

MADIREL (UMR 6121), Université de Provence-CNRS, Centre St Jérôme, 13397 Marseille Cedex 20, France

## Abstract

We compare different methods for particle size determination in nanocrystalline anatase ($TiO_2$) powders: transmission electron microscopy (TEM), nitrogen adsorption measurements, mercury porosimetry, and X-ray diffraction (XRD). The main source of errors in TEM is the sampling of the powder population, whereas in XRD the deconvolution of peak broadening due to instrument, microstrains, and crystalline domain size is delicate and can lead to unreliable results. Different approaches including Scherrer and Williamson-Hall equations are discussed. The presence of mesopores due to agglomerate formation is clearly revealed in adsorption measurements and porosimetry.

---

## 1. Introduction

One of the very basic insights of the physics and chemistry of solids is that most properties depend critically on the size of a solid in one, two, or three dimensions. Size effects appear when the characteristic size of the solid is reduced to a point where critical length scales of physical phenomena, such as a coherency length, a screening length, mean free paths for electrons or phonons, etc., become comparable. Typical examples of such relations are the domain size dependence for ferroelectric or ferromagnetic materials[1] or the change of color of semiconductor nanoparticles if their size is reduced to a few nanometers.[2]

The synthesis of materials with optimized properties by controlled manipulation of their microstructure on the atomic level is an emerging and rapidly growing interdisciplinary field.[3] Apparently simple and yet by no means fully investigated examples of such "nanomaterials" are nanocrystalline powders, which can be defined as granular materials with a mean particle size below 100 nm and a size distribution around this value. The particle size distribution is of paramount importance for various properties of this type of sample including catalytic and photocatalytic effects, optical and electrical properties, and magnetism. A reliable and well-mastered particle size analysis is therefore necessary, but not trivial for particle sizes in the nanometer range and where broad size distributions exist.

Several techniques are available to characterize nanocrystallite size and shape, including optical absorption spectroscopy, gas adsorption, X-ray diffraction (XRD), low-frequency inelastic Raman scattering, small-angle X-ray scattering, dark-field electron microscopy, high-angle annular dark-field electron scattering, and high-resolution

transmission electron microscopy (TEM).[4-9] The particle size determination can be based on (i) direct observation of particles, in the nanometer range especially by TEM, (ii) measurements of the coherence length of the particles, e.g., by XRD, where the particle size is related to the diffraction peak broadening, or (iii) determination of thermodynamic properties directly related to the surface area of the particles; the most prominent examples are the surface area determination by gas adsorption and by liquid intrusion (mercury porosimetry).

Each of these techniques has its advantages, but can also present artifacts, so that a comparison appears most suitable to determine the true particle size distribution of a powder population. An overview of recent literature shows few examples of such comparisons of different experimental techniques for particle size determination. One can cite, for example, correlations between high-resolution TEM, small-angle X-ray, and low-frequency inelastic Raman scattering.[9] A sophisticated image analysis of high-resolution TEM micrographs was also developed.[10] A discussion of the sources of error and the respective advantages/disadvantages of the techniques is often avoided. This situation was the starting point of our study: its objective is to compare the techniques mostly used for particle size determination, especially for the nontrivial case of nanocrystalline powders. In this study, TEM, XRD, gas adsorption, and mercury porosimetry techniques have been applied to characterize the particle size and particle agglomeration. The point of the present work is to benefit from the complementary nature of these four methods to study the particle size distribution.

The investigation was performed on phase-pure nanocrystalline anatase ($TiO_2$) as a model material. Anatase has many exciting applications in the field of energy and the environment, which are directly related to the particle and/or pore size: one can mention the photoelectrochemical properties used in dye-sensitized solar cells[11] or the photocatalytic properties used for water decontamination and self-cleaning devices.[12] Furthermore, the electrical properties of anatase are critically dependent on the particle size.[13]

## 2. Experimental Section

The anatase powders were prepared by the sulfate route.[14] In this process, the mineral precursor was dissolved in sulfuric acid and the titanium sulfate solution was then hydrolyzed by heating to 95-110 °C. The hydrolysis product was filtered and the filtrate was thoroughly washed until neutral pH was obtained. It was then calcined under air for 1 h at temperatures between 300 and 1100 °C to obtain a well-defined particle size distribution. Samples calcined at 300, 600, 700, and 800 °C will be particularly considered in the following, and are called samples A-D, respectively. The obtained powders were chemically analyzed by gravimetric techniques and ICP emission analysis. The concentrations of various impurities are given in Table 1 (total impurity content ~0.25 mol %).

The particle and pore size determination was based on four complementary techniques. First, the particle size distribution was determined by TEM observations. The transmission electron microscope (JEOL 2010 F) was equipped with a field emission gun and was operated at 200 kV (point resolution 0.18 nm). Electron diffraction (ED) patterns were recorded to confirm the phase-purity of the samples and the absence of rutile phase. TEM samples were prepared as follows: the anatase powder was ultrasonically dispersed for 3 h in absolute ethanol and afterward deposited on a carbonated copper grid. Quantitative measurements of size distribution were carried out by image analysis with a two-step procedure.[15] (*i*) Due to low contrast variations within TEM images, tested commercial

software was unable to find a large number of particles. In this context, particles were manually selected. (*ii*) The free software "Image Tool" was then used to perform image analysis. The distribution was investigated on the major axis length. To get statistically significant results, analysis was performed on more than 100 particles.

Second, adsorption measurements were performed at -196 °C using nitrogen as test gas in a commercial apparatus (ASAP 2010 Micromeritics). The sample was initially outgassed under a pressure of $10^{-2}$ Pa at a temperature of 140 °C for 1 h. Furthermore, mercury porosimetry experiments were performed using an Autopore II 9220 Micromeritics apparatus.

Third, X-ray powder diffraction (XRD) was performed in the classical Bragg-Brentano θ-2θ geometry (Siemens D5000 diffractometer) using Cu $K\alpha_1$ radiation ($\lambda$ = 0.15406 nm), a LiF crystal monochromator, and Soller slits. The experimental conditions of acquisition were fixed as 0.02° by step and 5-s accumulation time in the 2θ range 20-103°. To assess the instrumental line broadening, the XRD pattern of a standard microcrystalline rutile powder was recorded. The "Powder Cell" freeware v. 2.4 (Kraus, W. and Nolze, G., FIMRT, Berlin) was used to fit the data (Rietveld procedures) and to correct the residual Cu $K\alpha_2$ radiation. Peak profiles were assumed as pseudo-Voigt.

# 3. Results

**Determination of Particle Size Distribution by Transmission Electron Microscopy.** Figure 1A*i*-D*i* (*i* = 1, 2, 3) show typical TEM images and corresponding ED patterns of $TiO_2$ powder samples as a function of calcination temperatures (300, 600, 700, and 800 °C). Particle size distributions are presented in Figure 2A-D.

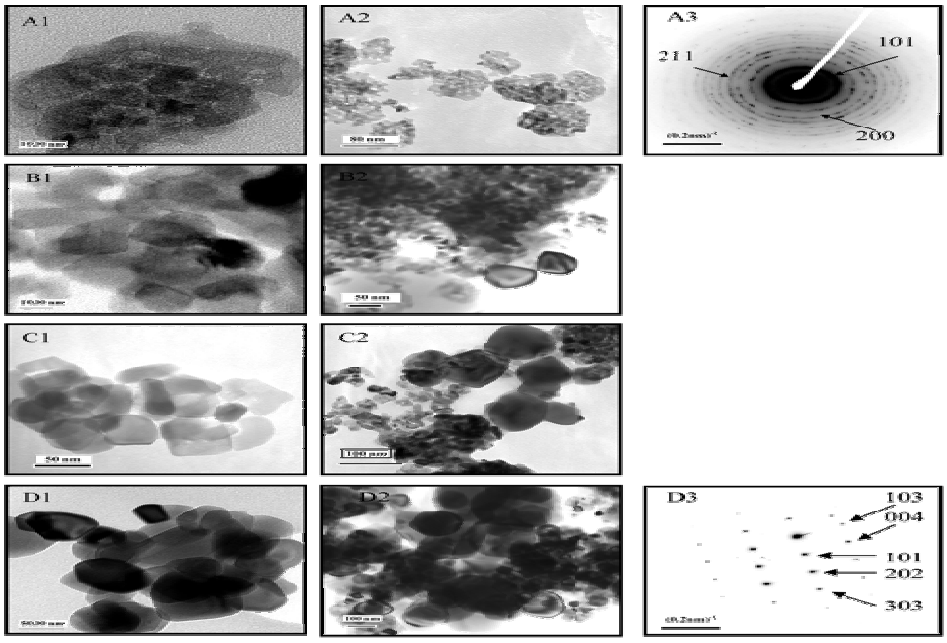


Figure 1 Transmission electron micrograph and corresponding electron diffraction patterns for powder samples A-D calcined at 300, 600, 700, and 800 °C.

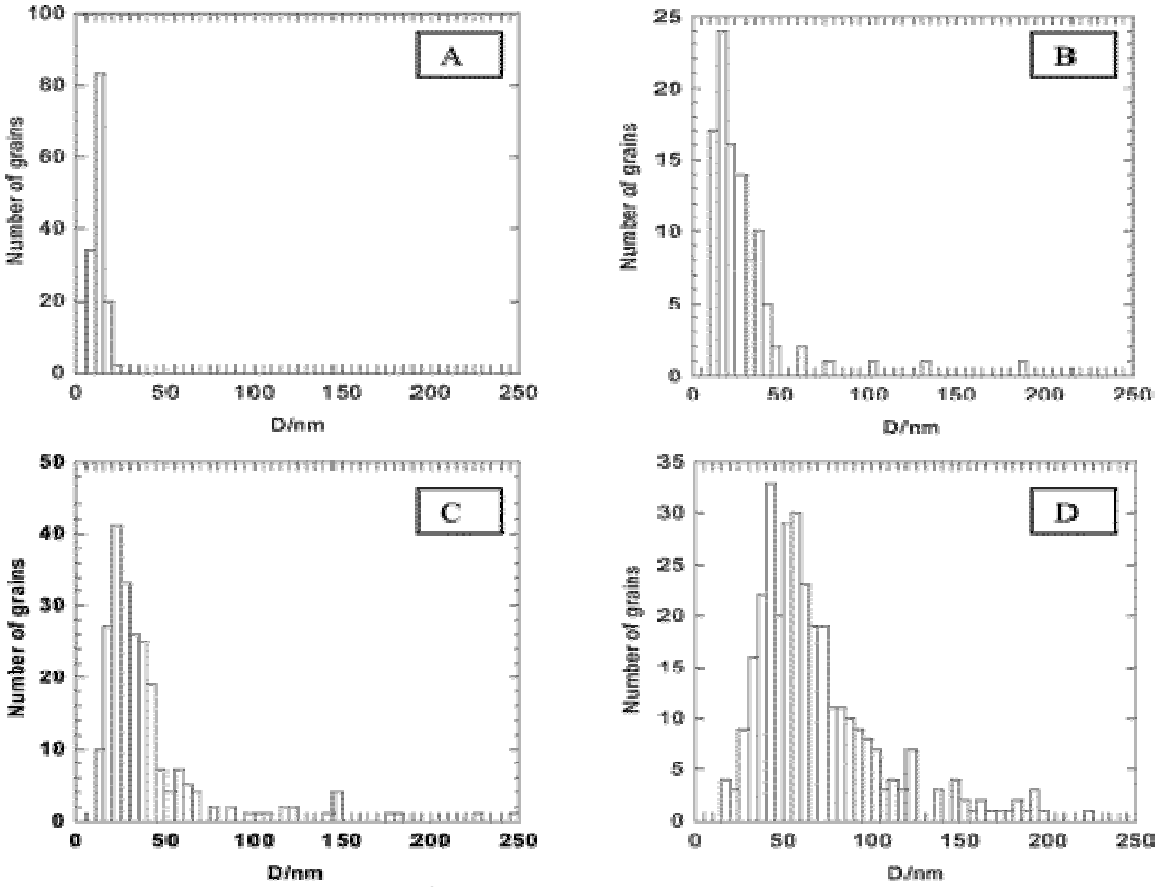

Figure 2 Particle size distributions for powder samples A-D.

In the case of the sample calcined at 300 °C (sample A), a narrow distribution is deduced: the particle size domain ranges from 5 to 20 nm with an average value of 12 nm (Figure 2A). It is worth mentioning that particles are embedded in agglomerates with a broad distribution (Figure 1A2) from 30 to 200 nm. ED patterns of agglomerates are characteristic of pure anatase phase (Figure 1A3).

As expected, Figures 1B1, C1, and D1 show clearly an increase of the average particle size with calcination temperature. Size distributions (Figure 2B-D) shift to larger average values (Table 2⊙) and broaden monotonically and asymmetrically for samples calcined from 600 to 800 °C (TEM size histograms 2C and D are well approximated by log-normal distributions). For samples heated at 600 °C, domain size ranges, on one hand, from 10 to 50 nm, which contains the major part of the agglomerated particle population. On the other hand, a few isolated particles have sizes around 100 nm (Figure 1B2), which can be due to a coalescence of primary particles in agglomerates. Grain boundary formation between particles embedded in agglomerates is clearly observed (Figure 1B1). At 700 °C, the particle size domain ranges from 20 to 80 nm with an average of 35 nm (Figure 2C). It is important to notice that the 100-nm particles population is confirmed (Figure 1C2).

Electron diffraction patterns of 200-nm particles after calcination at 800 °C, present typical (101), (103), and (004) reflections of the anatase phase (Figure 1D3). No rutile phase is detected up to 800 °C. This result is in good agreement with the XRD analysis developed in the third part. The particle size distribution (Figure 2D) is characterized by a large domain from 30 to 200 nm (Figure 1D2), which corresponds to agglomerate sizes previously observed

at 300 °C. One can notice that the coalescence of small primary particles in agglomerates leads to extinction of the particle population below 20 nm.

The large broadening is related to the particle growth and sintering processes in order to minimize the excess interfacial free energy, which is proportional to $2\gamma/R$ for spherical particles of radius $R$. $\gamma$ is the specific interfacial free energy, equal to the surface energy of the solid in equilibrium with the surrounding gas atmosphere in case of particle growth. In case of grain boundary formation, $\gamma$ is the boundary energy of the solid in equilibrium with a solid of same composition and structure. Particle sintering and growth depend on the number of neighbor particles in contact (i.e., the particle coordination number *cn*), which can coalesce to form, *in fine*, a unique big particle. A dispersion of *cn* and of agglomerate size in the precursor powder lead to a progressive distribution of particle size as the calcination temperature increases, i.e., at 600, 700, and 800 °C.

As a first conclusion of the TEM image analysis, in case of largely distributed particle size batches (20-200 nm), i.e., powders calcined at 600, 700, and 800 °C, imaging at different scales is needed to estimate correctly the proportion of small particles (10-60 nm in diameter) embedded in agglomerates (30-200 nm in diameter) and the proportion of large particles (120-200 nm in diameter). Furthermore, the particle overlapping in agglomerates leads to quite noisy images making the determination of proportion and size of the smallest particle population a very difficult task.

**Adsorption Measurements under Nitrogen and Mercury Porosimetry.** Figure 3 shows the adsorption isotherms obtained for powder samples A, B, and D ($P^\circ$ = 1.013 bar). Applying the BET (Brunauer, Emmett, and Teller) model, the specific surface area of a solid sample in contact with the gas phase can be calculated using linear regression in the low-pressure range[16] (unit $m^2/g$). The BET surface area $S_{BET}$ can be written as the total surface area of the powder population divided by the powder mass (eq 1).[17] The factor 6 applies for spherical as well as for cubic particles. The surface and the mass of each individual particle are related to its size $D_i$, as shown in eq 1. $\rho$ is the experimental density of the solid. Classically, the BET surface area is also related to the average particle size $D_{BET}$, as follows:

$$S_{BET} = 6\frac{\sum_i N_i D_i^2}{\rho \sum_i N_i D_i^3} = 6\frac{1}{\rho D_{BET}} \qquad (1)$$

The specific surface area for the different powder samples can be calculated using eq 1 and the discrete particle size distributions obtained from TEM images (Figure 2A-D). Table 2 compares the calculated specific surface area with the area obtained experimentally by adsorption measurements using nitrogen gas. The specific surface areas obtained from TEM size distribution and the BET experiments are in good agreement except for B and C batches, if we take into account in the calculation the few observed particles above 110 nm. The weighting of surfaces by the total particle mass in the BET calculation overemphasizes big particles that present a small specific surface area but contain a lot of matter. On the other hand, it confirms the underestimation of the small particle population by TEM analysis.

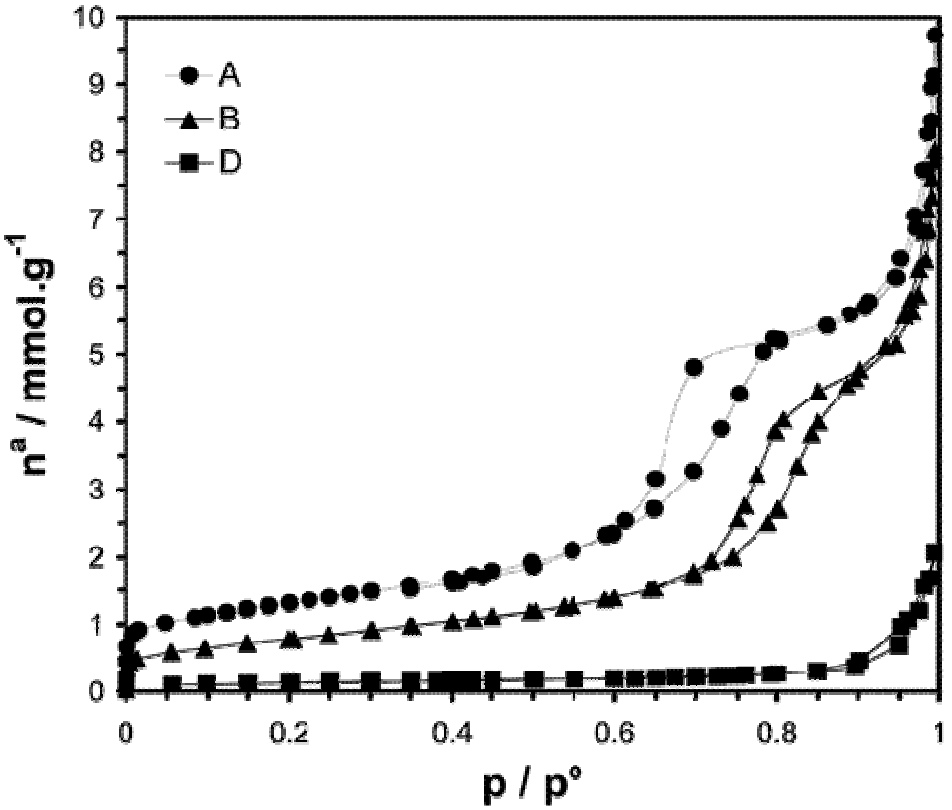

Figure 3 Nitrogen adsorption isotherms for powder samples A, B, and D.

One notices at higher relative pressure (above $P/P^\circ = 0.6$) in the adsorption isotherms a sudden increase of adsorbed nitrogen quantity followed by a "plateau". The observed hysteresis, especially for samples A and B, is characteristic of a mesoporosity[16] (pore diameter in the range 2-50 nm). We can apply the BJH (Barrett, Joyner, and Halenda) model[18] based on capillary condensation in mesopores described by the Kelvin eq 2

$$\ln(P/P^\circ) = -2\gamma V/(rRT) \qquad (2)$$

In this equation, $\gamma$ is the surface energy of the liquid at the adsorption temperature $T$, $r$ is the curvature radius of the liquid meniscus (which is related to the pore size), and $V$ is the molar volume of the liquid. For nitrogen adsorption at 77 K, one obtains an empirical equation[16]

$$r/\text{nm} = -0.415/\log(P/P^\circ) \qquad (3)$$

We can estimate the mesopore size distribution using the plot given in Figure 4. Here, the derivative of the cumulative volume $V_c$ by the pore size $D_p$ is plotted versus $D_p$. For sample A, a mean pore size of (6 ± 2) nm is obtained. The hysteresis in Figure 3 is shifted to higher pressures for sample B, corresponding to a larger mean pore size of (9 ± 4) nm. In case of sample D, no mesoporosity remains. Furthermore, the total mesopore area and the specific surface area $S_{BET}$ are almost equal for samples A and B. This implies that the particles do not contain any microporosity.

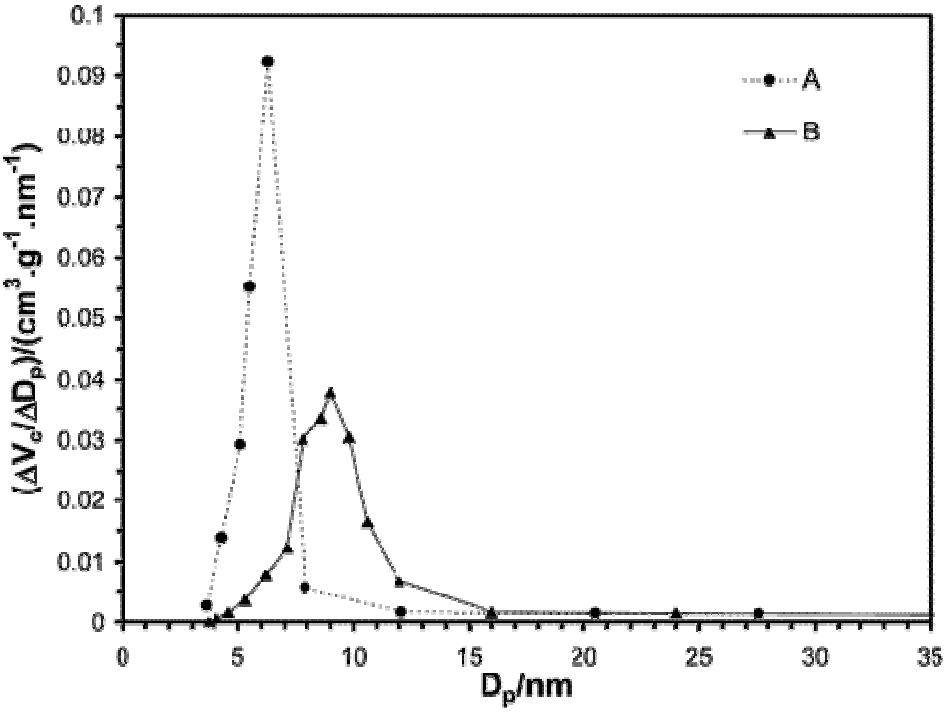


Figure 4 Pore size distribution for samples A and B, obtained using the BJH model.

The mercury porosimetry results for powder specimens A and D are shown in Figure 5. In very good agreement with the nitrogen absorption measurement, an average pore size around 7 nm is observed in sample A. In the perspective of TEM observations (see Figure 1A2, B2), the mesoporosity in sample A and B can be attributed to interparticle porosity in agglomerates (i.e., intra-agglomerate porosity). Following this, the shoulder at higher pore radius for sample A in Figure 5 must be due to the inter-agglomerate porosity, which appears distributed between 10 and 100 nm. A schematic representation is given in Figure 6. This means and confirms the preliminary TEM observations in sample A, that the particle agglomerates are very distributed in size from 30 to 200 nm. When the temperature of calcination increases, particle growth and particle boundary formation are activated, leading to a progressive coalescence of primary particles inside agglomerates, consistent with sintering theory.[19] At 800 °C (sample D), most agglomerates have coalesced giving a broad particle size dispersion, which reflects the primitive agglomerate size distribution.

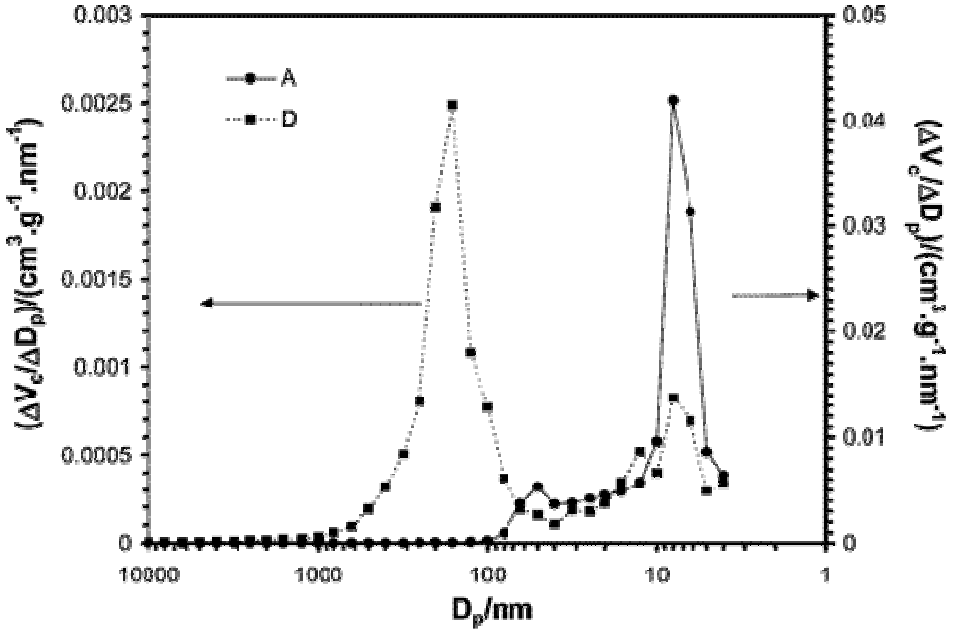


Figure 5 Mercury porosimetry for powder samples A and D. Note that there is almost 1 order of magnitude between the two ordinates.

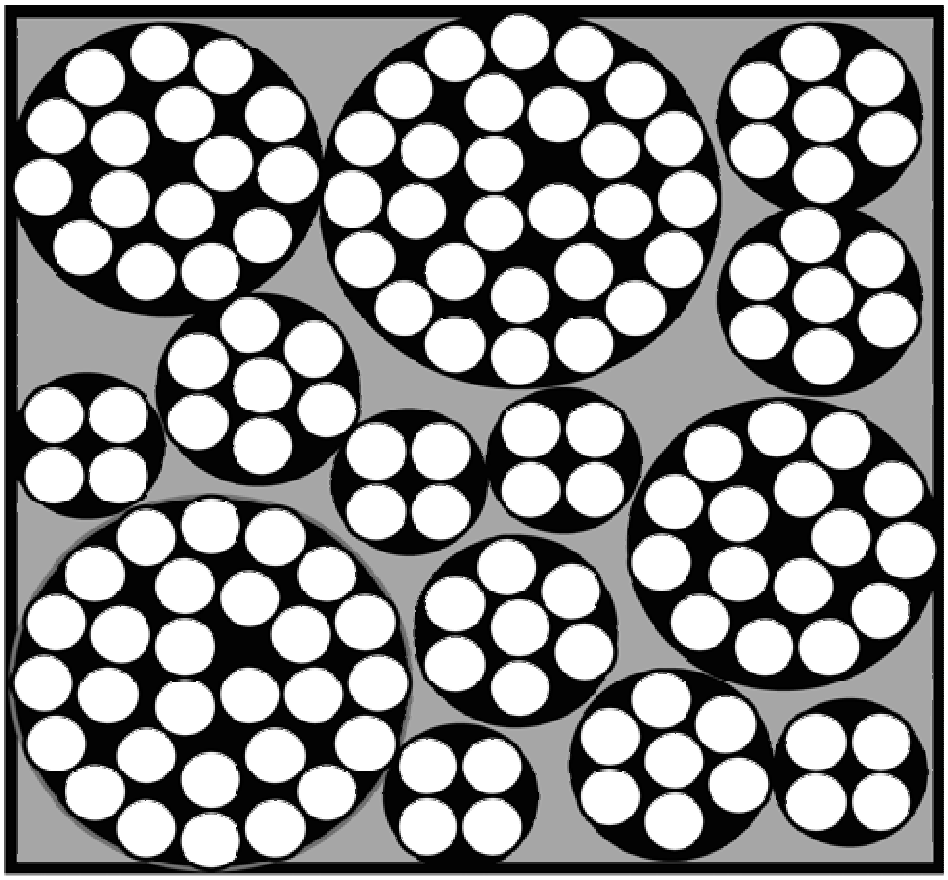

Figure 6 Schematic model showing intra- and inter-agglomerate porosity in sample A.

**Determination of Particle Size and Microstrain by XRD.** Figure 7 shows the refinement of peaks when the calcination temperature increases. These XRD patterns confirm, in agreement with TEM, that up to 800 °C calcination temperature, anatase remains phase-pure without any indication of rutile phase.

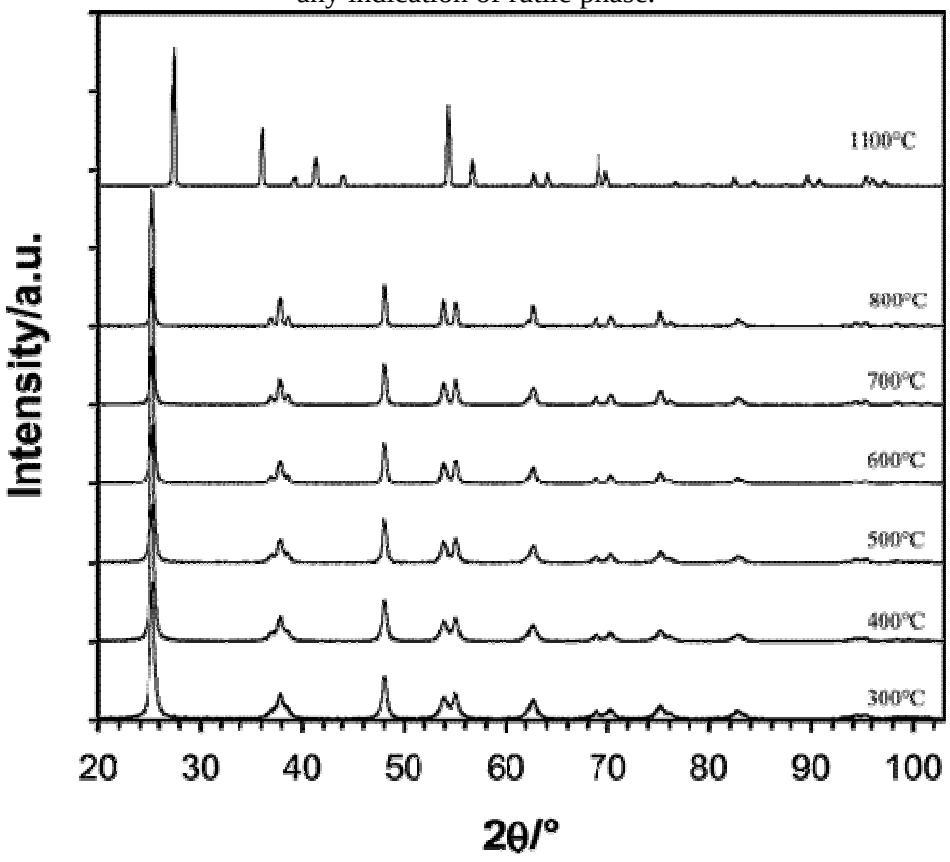


Figure 7 X-ray diffraction patterns of $TiO_2$ powders calcined at 300-1100 °C.

In the diffraction pattern, peak broadening is due to four factors: microstrains (deformations of the lattice), faulting (extended defects), crystalline domain size, and domain size distribution. If we assume that analyzed $TiO_2$ crystals are free of strains and faulting, peak broadening is only due to crystalline domain size D, which can then be calculated by the Scherrer formula:[20,21]

$$D = K\lambda/[W\cos(\theta)] \qquad (4)$$

*K* is a constant which depends on the particle morphology and varies from 0.89 to 1.39 rad. In the following, we use consistently $K = 1$, which corresponds to an average volume of the apparent size *D* independently of a peculiar morphology.[22] $\lambda$ is the Cu K$\alpha$ radiation (in nm), *W* is the full width at half-maximum (fwhm in radian), and $\theta$ is the diffraction angle (deg).

An additional instrumental broadening, arising from slit width, penetration in sample, imperfect monochromaticity, and imperfect focusing is generally observed. For a detailed analysis and comparison of peak broadening and data processing, see the review by Balzar.[23] To deconvolute size and instrumental effects, two simplified methods are generally applied, Cauchy (eq 5) or Gauss approximation (eq 6), depending on the assumed mathematical profiles describing the two effects i.e., Lorentzian or Gaussian, respectively.

$$W = \mathrm{fwhm}_{\mathrm{sample}} - \mathrm{fwhm}_{\mathrm{standard\ reference}} \qquad (5)$$

$$W = (\mathrm{fwhm}^2_{\mathrm{sample}} - \mathrm{fwhm}^2_{\mathrm{standard\ reference}})^{1/2} \qquad (6)$$

To correct the instrumental broadening, we used two approaches. (1) The classical approach, in which the instrumental broadening is given by the X-ray diffraction pattern of a standard microcrystalline rutile sample (Figure 7, 1100 °C batch), in which the particle size (2 μm) is large enough to eliminate particle-size and microstrain broadening. The fwhm of rutile peaks as a function of 2θ is very well described by Cagliotti's law.[24] (2) A linear regression of experimental fwhm for the (101) reflection of anatase has been plotted as function of the inverse BET value $1/D_{\mathrm{BET}}$ (Figure 8a). Value of experimental fwhm is deduced, for microcrystalline sample, from the intercept. Afterward, Gauss and Cauchy approximations are calculated in Figure 8b. In our case, an excellent correlation is obtained with the Cauchy approximation. This effect can be explained by the crystallite size distribution in our batches.[25] On the other hand, the Gaussian profile is in good agreement with the experimental profile obtained with our standard rutile sample and in the literature the mostly used assumption is Gauss.[22]

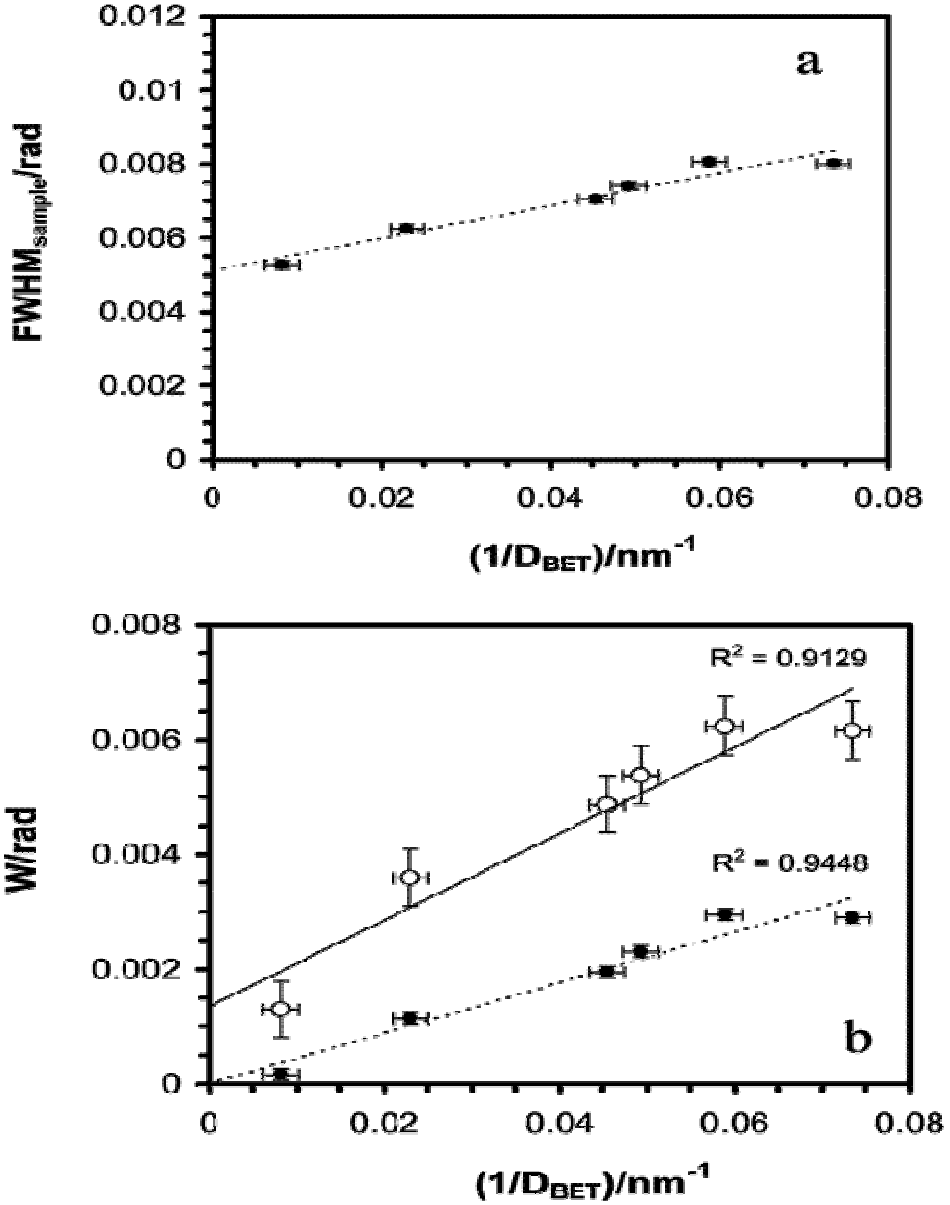


Figure 8 (a) Correlation of fwhm with the inverse particle size, obtained by BET experiments. (b) Gauss (open dots) and Cauchy (black marks) approximations.

---

Finally, we present the results obtained with the Gauss approximation using Cagliotti's equation. The results obtained with Scherrer's formula on (101) and (200) peaks are summarized in Table 3.

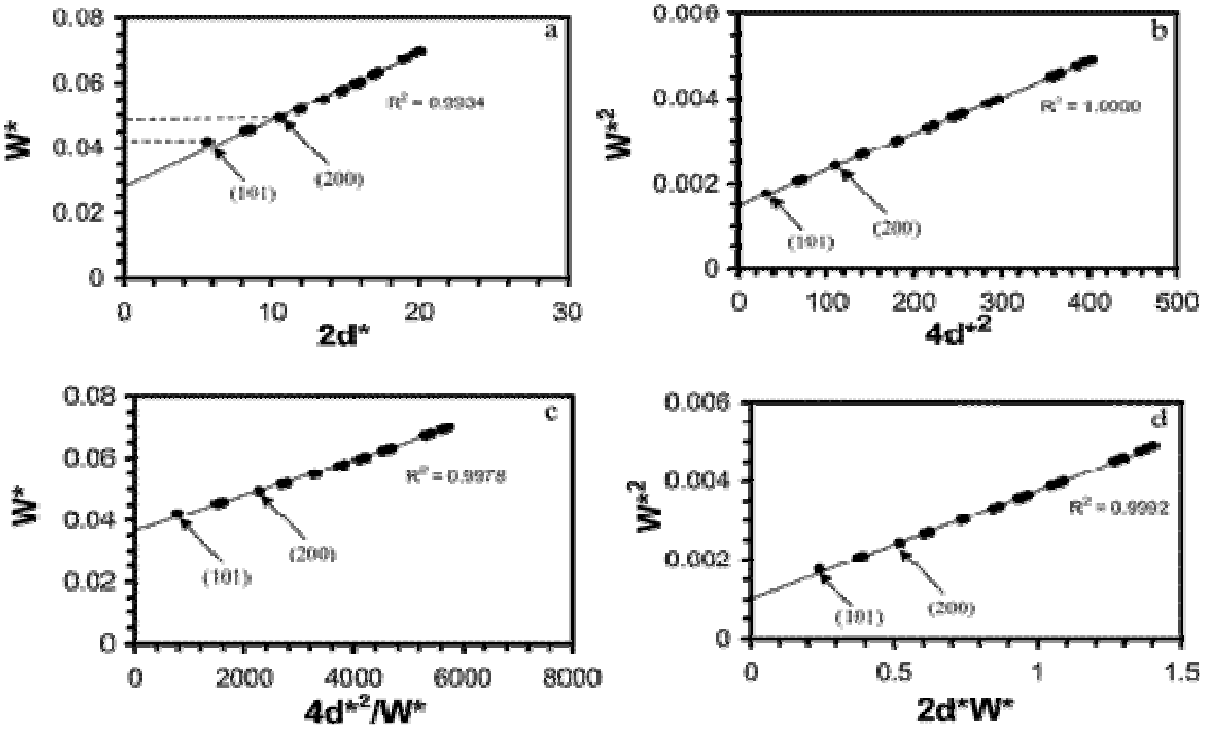


Figure 9 Deconvolution of strain and size effects using 4 different approximations, from top left to bottom right: (a) Cauchy-Cauchy, (b) Gauss-Gauss, (c) Cauchy-Gauss, and (d) Gauss-Cauchy (cf. Table 4).

The additional line broadening due to microstrain $\epsilon_S$ can be expressed according to Stokes and Wilson[23]

$$W_\epsilon = 4\epsilon_S \tan\theta \qquad (7)$$

Combining eqs 4 and 7, a separation of the two broadening effects is possible by the so-called Williamson-Hall plot of $W\cos\theta$ vs $\sin\theta$: [26]

$$W\cos\theta = \lambda/D + 4\epsilon_S \sin\theta$$

or more commonly in the reciprocal space

$$W^* = 1/D + 2\epsilon_S d^* \text{ with } W^* = W\cos\theta/\lambda \text{ and } d^* = 2\sin\theta/\lambda \qquad (8)$$

In this representation, $W$ is assumed to be the addition of the line broadening due to microstrains and due to particle size. Therefore, if we plot $W\cos\theta$ versus $\sin\theta$, microstrain is calculated from the slope and the particle size is obtained from the intercept. The linear additivity implies a Lorentzian shape for both broadening effects (Cauchy approximation). One can also consider three other cases, i.e., Gauss-Gauss, Gauss-Cauchy, or Cauchy-Gauss deconvolution for the two effects (the equations are summarized in Table 4). An example of "Williamson-Hall" plot for the smallest particles (sample A) using the four different deconvolutions is shown in Figure 9. One can notice a very good linear dependence of the experimental points, especially with the Gauss-Gauss approximation. The results for different powder batches using Gauss-Gauss approximation are compiled in Table 3.

One can conclude that consistent results are obtained using the Scherrer equation, corrected by BET data, and the Williamson-Hall (W-H) equation, except for the 800 °C sample D where the experimental uncertainty is much larger. It is worth knowing that the Scherrer formula is valid as long as the particle size is smaller than 100 nm. The Williamson-Hall determination for sample D is very well correlated with the average TEM values (cf. Table 2). From the Williamson-Hall equation, we can also determine the average microstrain distribution $\varepsilon_s$. The order of magnitude of $\varepsilon_s$ is in agreement with the values determined by Bregani et al.[27] We observe that $\varepsilon_s$ decreases with increasing particle size above 600 °C. An isotropic strain only shifts the peak position (correlated to the homogeneous cell parameter evolution as a function of stress). Therefore, this size dependence of $\varepsilon_s$ could be related to a "skin" effect due to a stoichiometry evolution from the surface to the bulk of $TiO_{2-x}$ well-known for oxide materials.[28] The thickness of the "skin" (space charge region), $\delta$, where the cell parameter is variable due to microstrain distribution, may be crystallite size independent, proportional to $\delta/D$. The linear variation of $\varepsilon_s$ as function of the inverse average particle diameter shown in Figure 10 is in agreement with this kind of explanation.

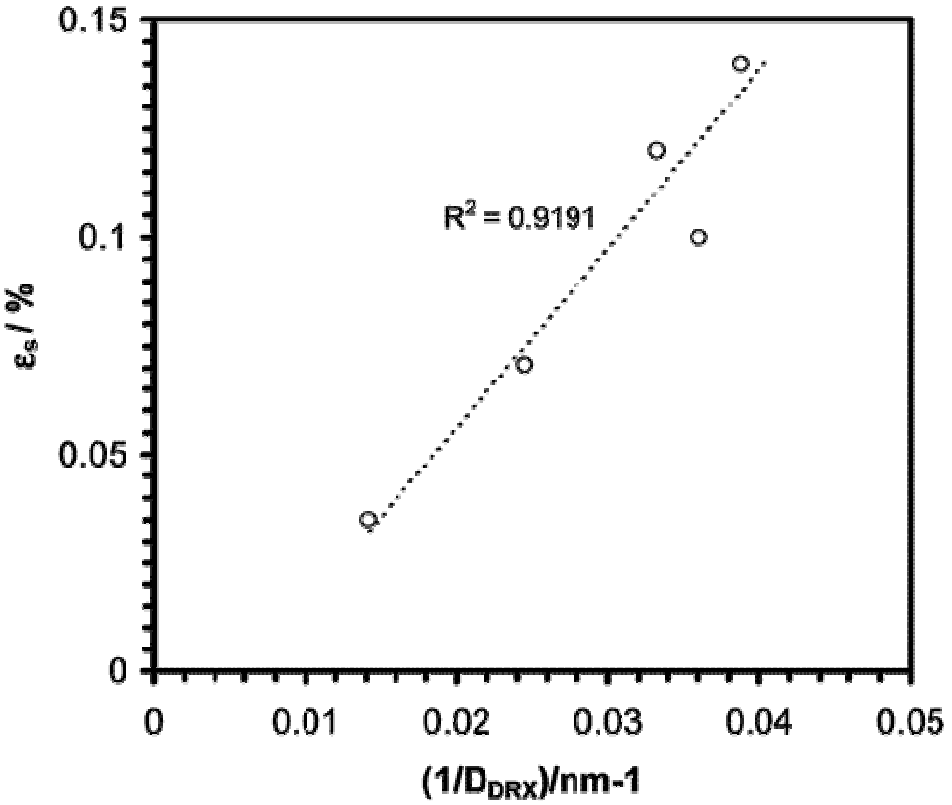


Figure 10 Microstrain calculated using Williamson-Hall equation as function of the inverse particle size.

## 4. Discussion

One notices globally a satisfactory agreement among the average particle size values from TEM, BET, and XRD. However, let us discuss the respective advantages and disadvantages

of the three techniques. TEM analysis provides direct information without hypothesis on crystalline domain shape. The advantage of TEM is clearly the visualization of objects and structures, here anatase single crystals, allowing counting of discrete objects and direct deduction of a statistical particle size distribution. However, possible artifacts are related to the sampling of the powder population including the choice of the investigated objects. Furthermore, the size distribution obtained from TEM can be unreliable due to the difficulty in counting small particles (contrast problems, large particles will be counted more easily) and also where the separation between crystallites is unclear, e.g., in case of agglomerated particles, containing in reality several smaller particles (e.g., Figure 1A). The gas adsorption technique is very sensitive to small particles (large surface!) and to inter- and intra-granular porosity. This can induce a large error for powder populations with a large size distribution and important agglomeration. One remarks discrepancies between BET calculation and TEM observation for the most distributed samples C and D (Table 2). Moreover, standard measurements using nitrogen gas induce a supplementary uncertainty related to the nonspherical nitrogen molecule that is polarizable on charged surfaces (induced dipole interaction), which can generally be expected for an ionic solid, such as titanium dioxide. The surface occupied by a nitrogen molecule can vary substantially, depending on its orientation (vertical or horizontal). It can therefore be more favorable in certain cases to use a spherical atom, such as argon, to do adsorption measurements. The XRD technique requires several corrections and deconvolutions to reach reliable particle size values: the presence of $K\alpha_2$ radiation and instrumental line broadening have to be taken into account. Ionic systems commonly exhibit no stacking faults and a small amount of strain. The Williamson-Hall approach taking the strain effects explicitly into account works better for the largest sample D. To separate strain and size broadening effects, a Gaussian deconvolution gives the best results. Generally, only a complex mathematical modeling of the experimental data, introducing explicit profiles of particles size distribution can allow extraction of statistical parameters from averaged information about a particle population.

## 5. Conclusion

We have investigated various particle size determination methods (TEM, BET, and XRD) for the specific case of nanocrystalline powders, here single-phase anatase with mean particle size between 12 and 120 nm. We have shown that all techniques have their respective advantages, but can also produce specific artifacts. It is also important to keep in mind that each specific technique requires discussion of sampling and statistics.

The advantage of TEM is the direct observation. However, small particles may be overlooked or can be difficult to distinguish in agglomerates. The advantage of BET is to give a global surface area value, from which an average particle size can be calculated assuming regular (cubic or spherical) and monodisperse particles. Scherrer's equation applied to fwhms of XRD peaks gives a crystallite size in relatively good agreement with TEM and BET. The coupling of the gas adsorption technique and the direct observation by TEM offers the advantage of a certain simplicity and a good correlation/complementarity of the information (specific area, mesoporosity, and microporosity on one side, and size, size distribution and agglomeration on the other one).

To limit the broadening of the particle size distribution with temperature, the precursor must be treated before calcination (by mechanical and/or chemical means) to reduce the

agglomerate size distribution. It is worthy to note that microcrystalline anatase particles are obtained under the thermal conditions of powder treatment presented in this work.

## Acknowledgment

We thank Drs. R. Denoyel (Madirel) and P. Bouvier (LEPMI, Grenoble, France) for fruitful discussions. A. Garnier (Madirel) and W. Saikaly (CP2M, Marseille, France) are gratefully acknowledged for technical support, respectively for the XRD and TEM experiments.

* To whom correspondence should be addressed. E-mail: rb@up.univ-mrs.fr.

1. Edelstein, A. S., Cammarata, R. C., Eds. *Nanomaterials: Synthesis, Properties and Applications*; Institute of Physics: Bristol, 2002.

2. Henglein, A. *Chem. Rev*. 1998, *89*, 1861.

3. Gleiter, H. *Acta Mater*. 2000, *48*, 1.

4. Roussignol, P.; Ricard, D.; Lukasik, J.; Klytzanis, C. *J. Opt. Soc. Am*. 1987, *4*, 5.

5. Williams, J. A.; Rindone, G. E.; McKinstry, H. A. *J. Am. Ceram. Soc*. 1981, *64*, 702.

6. Allais, M.; Gandais, M. *J. Appl. Crystallogr*. 1990, *23*, 418.

7. Liu, L. C.; Risbul, S. H. *J. Appl. Phys*. 1990, *68*, 28.

8. Degiogio, V.; Banfi, G.; Righini, G.; Rennie, A. *Appl. Phys. Lett*. 1990, *57*, 2879.

9. Champagon, B.; Andranasolo, B.; Ramos, A.; Gandais, M.; Allais, M.; Benoit, J. P. *J Appl. Phys*. 1993, *73*, 6.

10. Hytch, M.; Gandais, M. *Philos. Mag. A* 1995, *72*, 619.

11. O'Regan, B.; Grätzel, M. *Nature* 1991, *353*, 737.

12. Sakkas, V. A.; Albanis, T. A. *Appl. Catal. B* 2003, *46*, 175.

13. Knauth, P.; Tuller, H. L. *J. Appl. Phys*. 1999, *85*, 897.

14. Knauth, P.; Bouchet, R.; Schäf, O.; Weibel, A.; Auer, G. In *Synthesis, Functionalization and Surface Treatments of Nanoparticles*; Baraton, M.-I., Ed.; American Scientific Publishers: Stevenson Ranch: CA, 2002.

15. Nicolas, M. Ph.D Thesis, University Grenoble I, 2002.

16. Rouquerol, J.; Rouquerol, F.; Sing, K. S. W. In *Adsorption by Powders and Porous Solids*; Academic Press: London, 1999.

17. Allen, T. *Particle Size Measurement, Vol. 1*, fifth ed.; Kluwer Academic Publishers: Dordrect, The Netherlands, 1999.

18. Barrett, E. P.; Joyner, L. G.; Halenda, P. H. *J. Am. Chem. Soc.* 1951, *73*, 373.

19. Kingery, W. D.; Bowen, H. K.; Uhlmann, D. R. I*ntroduction to Ceramics*, second ed.; Wiley-Interscience Publications: New York, 1976.

20. Warren, B. E. *X-ray Diffraction*; Dover Publications: New York, 1969.

21. Scherrer, P. *Gött. Nachr*. 1918, *2*, 98.

22. Klug, H. P.; Alexander, L. E. *X-ray Diffraction Procedures for Polycrystalline and Amorphous Materials*, second ed.; Wiley-Interscience Publications: New York, 1974.

23. Balzar, D. *Defect and Microstructure Analysis from Diffraction*; Oxford University Press: New York, 1999.

24. Caglioti, G.; Paoletti, A.; Ricci, F. P. *Nucl. Instrum*. 1958, *3*, 223. 25. Alexander, L. E. *J. Appl. Phys.* 1948, *19*, 1068.

26. Williamson, G. K.; Hall, W. H. *Acta Metal.* 1953, *1*, 22.

27. Bregani, F.; Casale, C.; Natali-Sora, I.; Robba, D.; Sangaletti, L.; Toledo, G. P. *Sens. Actuators, B* 1996, *31*, 25.

28. Guo, X.; Sigle, W.; Fleig, J.; Maier, J. *Solid State Ionics* 2002, *154-155*, 555.

Table 1. Gravimetric and ICP Analysis of Impurities in Anatase ($TiO_2$) Samples[a]

| | concentration/ppm | |
|---|---|---|
| element | ICP | gravimetry |
| Na | 930 | 1200-1300 |
| Si | 200 | 385 |
| S | 410 | 270 |
| | | |

[a] Other: P, 270; Zr, 175; Nb, 68; Mg, 21; Al, 13; V, 9; Fe, 8; Pb, 5; Ba, 4; Cr, 3; Zn, 3; Cu, 2; Ni, Co, Mn < 1

Table 2. Experimental and Calculated (Eq 1) BET Surface Areas; Average Particle Sizes Calculated from BET Data (Eq 1) and Observed by TEM

| temp °C | $S_{BET}$, exp $m^2/g$ | $S_{BET}$, calc $m^2/g$ | $D_{BET}$ nm | $D_{TEM}$ nm |
|---|---|---|---|---|
| 300 | 115 | 114 | 13 ± 1 | 12 ± 3 |

| | | | | |
|---|---|---|---|---|
| 600 | 71 | 50[a] | 22 ± 2 | 24 ± 10 |
| 700 | 35 | 30[a] | 45 ± 4 | 35 ± 15 |
| 800 | 13 | 14 | 120 ± 10 | 70 ± 35 |

[a] The given value was obtained without taking into account the small particle population over 110 nm.

Table 3. Comparison of XRD Results Using Gauss Correction for Instrumental Broadening[a]

| | Reference: microcrystalline rutile | | | | Reference: BET data | |
|---|---|---|---|---|---|---|
| | Williamson-Hall | | Scherrer | | Scherrer | |
| temp/°C | *D*/nm | $\varepsilon_S$ | *D*(101)/nm | *D*(200)/nm | *D*(101)/nm | *D*(200)/nm |
| 300 | 26 ± 5 | 0.0014 | 24 ± 5 | 20 ± 5 | 25 ± 8 | 22 ± 8 |
| 400 | 26 ± 5 | 0.0014 | 24 ± 5 | 20 ± 5 | 25 ± 8 | 22 ± 8 |
| 500 | 28 ± 5 | 0.0010 | 27 ± 5 | 23 ± 5 | 29 ± 8 | 25 ± 8 |
| 600 | 30 ± 5 | 0.0012 | 29 ± 7 | 24 ± 6 | 32 ± 9 | 26 ± 9 |
| 700 | 41 ± 8 | 0.00071 | 37 ± 9 | 33 ± 8 | 44 ± 12 | 40 ± 12 |
| 800 | 71 ± 15 | 0.00035 | 58 ± 15 | 53 ± 12 | 121 ± 40 | 103 ± 40 |

[a]The uncertainty takes into account the background and the $K\alpha_2$ corrections (errors between 15 and 20%) and the data fitting by pseudo-Voigt functions (between 3 and 10%).

Table 4. Equations Used for Deconvolution of Size and Strain Effects

| convolution hypothesis of size and strain effects | equation |
|---|---|
| Cauchy-Cauchy | $W^* = 1/D + \varepsilon_S 2d^*$ |
| Cauchy-Gauss | $W^* = 1/D + 4\varepsilon_S^2 d^{*2}/W^*$ |
| Gauss-Gauss | $W^{*2} = 1/D^2 + 4\varepsilon_S^2 d^{*2}$ |
| Gauss-Cauchy | $W^{*2} = 1/D^2 + \varepsilon_S 2d^* W^*$ |